Stability of reaction-fronts in porous media

Magnus Wangen[a,*]

[a] *Institute for Energy Technology, P.O.Box 40, N-2027 Kjeller, Norway, tel: +47-6380-6259, fax: +47-6381-5553*

Abstract

The stability of reaction-fronts in porous media is studied with analytical and numerical methods. A stability criterion has been derived using linear stability analysis assuming a sharp font. The sharp front assumption is an approximation of the mathematical model in the limit of an infinite rapid reaction. The criterion shows that the stability of a sharp reaction front is dependent on the permeability that develops behind it. The sharp front is unstable for perturbations of any wave-length if the permeability increases behind the front. The criterion shows that short wave-length perturbations are more unstable than long wave-length perturbations. The sharp front is labile when the permeabilities are the same at both sides of the front. This means that the perturbed front moves unchanged forward. Finally, perturbations will die out in case the permeability decreases behind the sharp front. The stability of non-sharp fronts are simulated numerically when dissolution is by first order kinetics, the transport is by convection and diffusion and when the permeability and specific reactive surface depends on the porosity. The numerical experiments behave according to the stability criterion.

*Corresponding author
Email address: Magnus.Wangen@ife.no (Magnus Wangen)

Keywords: reaction-fronts in porous media, stability criterion, linear stability analysis

1. Introduction

The injection of a reactive fluid into a porous medium leads to alteration of the reactive part of the solid rock matrix and to changes of the porosity and permeability. Familiar examples are the dissolution of the matrix and increasing porosity in carbonate rocks by CO_2 rich brine Xu et al. [21, 22]. The entire rock matrix may also be dissolved with the results that "wormholes" develop Golfier et al. [8]. Under certain conditions of flow and reaction the alteration pattern becomes a reaction front. The front is a transition from fully reacted to unreacted rock over a "short" distance. The reactive part of the matrix has fully reacted behind the front and it is unreacted ahead of the front.

Laboratory experiments and simulation studies have shown numerous examples of reaction fronts that develop in an unstable manner Golfier et al. [8]. Small perturbation on a linear front develops into fingers Ortoleva et al. [14]. The stability of such reaction fronts has been studied by Chadam et al. [3, 4], Ortoleva et al. [14], Xin et al. [20] and more recently by Zhao et al. [23]. Through a linear stability analysis these authors obtained a critical pressure gradient as a condition for stability, where the critical gradient is a function of the ratio of permeabilities ahead of and behind the front. The linear stability analysis was based on a sharp front in the porosity and permeability, but not the concentration. Hirch and Bhatt [9] obtained analytical results for the linear stability of reaction fronts in the cases of small and large wave numbers, and small variations in the permeability. They are building on the work of Sherwood [17] and they take into account that the front has finite width.

Here we suggest a simpler linear stability analysis than the one developed by Chadam

et al. [3], Sherwood [17], Ortoleva et al. [14], Chadam et al. [4], Hirch and Bhatt [9], Xin et al. [20]. It is derived for the limit of a sharp front (zero width), where the porosity, permeability and concentration are step-functions. The derivation follows the same line of reasoning as applied to the stability of the interface between two immiscible fluids during vertical displacement in a Hele-Shaw cell, as for instance shown by Marle [11]. This analysis gives a simple condition for the stability of sharp fronts in terms of the permeabilities at the two sides of the front. The stability criterion shows that the stability of a sharp front depends on the permeability that develops behind the front. It does not involve a critical pressure gradient that in turn depends on the ratio of the permeabilities of the two sides of the front, as shown by Chadam et al. [3], Ortoleva et al. [14], Chadam et al. [4], Xin et al. [20]. Furthermore, the analysis presented here shows in a simple way how the stability depends on the wave length of the front perturbation.

The stability of non-sharp fronts are studied numerically when dissolution is by first order kinetics, the transport of dissolved matter is by convection and diffusion and when the permeability and specific reactive surface depend on the porosity. The sharp front assumption is an approximation of the mathematical model in the limit of an infinite rapid reaction. Numerical solutions of the mathematical model demonstrate the different cases of stability when the reaction is restricted to a narrow zone.

The paper is organized as follows: The numerical model is first explained and the assumptions about permeability and the specific surface area of the rock are then discussed. The stability criterion of sharp reaction fronts is presented, the derivation of the stability condition is given, before numerical examples of stable, labile and unstable fronts are shown.

2. The mathematical model

The mathematical model consists of three coupled macroscopic equations as shown by Ortoleva et al. [14], Chadam et al. [4], Xin et al. [20]. They are solved on a rectangular domain of length l_0, where the side at $x = 0$ is the inlet and the opposite side at $x = l_0$ is the outlet. The other sides are closed for fluid flow.

The first equation is the pressure equation that follows from conservation of fluid mass and Darcy's law (see Appendix A)

$$\nabla \cdot \left(\frac{\varrho_f \, k(\phi)}{\mu} \nabla p \right) = -(\varrho_s - \varrho_f) \frac{\partial \phi}{\partial t} \tag{1}$$

where ϕ is the porosity, ϱ_f is the fluid density, ϱ_s is the solid density, $k(\phi)$ is the permeability, μ is the viscosity and p is the fluid pressure. The fluid density is taken to be constant, independent of the concentration of the dissolved solid, since it is assumed that the concentration is low. The solid density is also taken to be constant. The pore space is assumed incompressible and the porosity is changing only because of chemical reactions. A constant fluid density also implies that the fluid pressure can be taken to be a fluid flow potential [1]. The pore space has an isotropic permeability $k(\phi)$, which changes with the porosity. The right-hand-side of equation (1) is a source term that expresses that the solid matrix being dissolved enters the fluid phase. It is shown in Appendix A that this source term has a negligible impact on the Darcy flow, and that it can be approximated by zero. Boundary conditions for pressure equation (1) are a constant volume flux at the inlet and zero pressure at the outlet. The initial fluid pressure is zero.

The dissolution of the porous matrix is modelled with a one-component reaction-transport equation

$$\frac{\partial (\phi c)}{\partial t} + \nabla \cdot \Big(c \, \mathbf{w} - \phi D \nabla c \Big) = k_d \, S(\phi) \Big(1 - \frac{c}{c_{\mathrm{eq}}} \Big), \tag{2}$$

where c is the concentration of the reactive species in the pore fluid (in units $\mathrm{mol\,m^{-3}}$) and $\mathbf{w} = -(k/\mu)\nabla p$ is the Darcy flux. The term in parentheses, after the divergence-operator, accounts for transport of the dissolved species by Darcy flow and by Fickian diffusion. The diffusivity in the fluid filling the pore space is denoted D (in units $\mathrm{m^2 s^{-1}}$). The right-hand-side is a reaction term, where dissolution is by first order kinetics. The reaction constant for dissolution is k_d (in units $\mathrm{mol\,s^{-1} m^{-2}}$), the specific (reactive) surface of the pore space is $S(\phi)$ (in units $\mathrm{m^2\,m^{-3}}$), and the specific reactive surface area changes with the porosity. The equilibrium concentration is c_{eq}. We notice that the right-hand-side is positive as long as $c < c_{\mathrm{eq}}$, and that it acts as a source term. The boundary conditions are $c = 0$ at the inlet and $c = c_{\mathrm{eq}}$ at the outlet and the pore fluid has initially $c = c_{\mathrm{eq}}$.

The third equation gives the rate of the change of porosity caused by the dissolution process as

$$\frac{\partial \phi}{\partial t} = \mathcal{V}_s k_d \, S(\phi) \Big(1 - \frac{c}{c_{\mathrm{eq}}}\Big), \tag{3}$$

where the $\mathcal{V}_s$ is the molar volume of the reactive solid (in units $\mathrm{m^3\,mol^{-1}}$). The three equations (1), (2) and (3) are the basis of the reaction-transport model.

It should be mentioned that the reaction-transport equation (2) can be approximated as

$$\phi \frac{\partial c}{\partial t} + \mathbf{w} \cdot \nabla c - \nabla \cdot \Big(\phi \, D \nabla c\Big) = \frac{1}{\mathcal{V}_s}\Big(1 - c\,\mathcal{V}_s \frac{\varrho_s}{\varrho_f}\Big)\frac{\partial \phi}{\partial t} \approx \frac{1}{\mathcal{V}_s}\frac{\partial \phi}{\partial t} \tag{4}$$

by use of the expression (1) for fluid conservation. See also equation (A.7) for conservation of fluid mass in Appendix A. The approximation on the right-hand-side follows from the assumption $c_{\mathrm{eq}}\mathcal{V}_s \ll 1$ since $0 \leq c \leq c_{\mathrm{eq}}$.

3. 1D dimensionless formulation

Reaction and transport is in the following studied in box with the length l_0, when it is flooded with an average Darcy flux u_{D0}. The average Darcy flux is simply the injection (volume) rate divided by the cross section of the box. Beware that alternative dimensionless formulations are based on a representative length scale at the pore level [8]. It is convenient to introduce the dimensionless variables $\hat{x} = x/l_0$, $\hat{t} = t/t_0$, $\hat{\phi} = \phi/\phi_0$ and $C = (c/c_{\rm eq} - 1)$, where t_0 is the characteristic time of diffusion

$$t_0 = \frac{l_0^2}{D}. \tag{5}$$

The initial porosity is ϕ_0. We notice that the dimensionless concentration is $C = -1$ when $c = 0$ and that it increases to $C = 0$ at the equilibrium concentration $c = c_{\rm eq}$. The dimensionless version of equation (2) is in 1D (along the x-axis)

$$\hat{\phi}\frac{\partial C}{\partial \hat{t}} + {\rm Pe}\,\frac{\partial C}{\partial \hat{x}} - \frac{\partial}{\partial \hat{x}}\Big(\hat{\phi}\frac{\partial C}{\partial \hat{x}}\Big) = -{\rm Da}\,C \tag{6}$$

where Péclet-number and Damköhler-number are defined as

$${\rm Pe} = \frac{l_0 u_{D0}}{\phi_0 D} \quad \text{and} \quad {\rm Da} = \frac{l_0^2 S\, k_d}{\phi_0 c_{\rm eq} D} \tag{7}$$

Both the ${\rm Pe}$- and the ${\rm Da}$-numbers include the initial porosity, since it is convenient with respect to the interpretation of the numbers in terms of the time scales involved. There are two more time scales in the 1D reaction and transport equation (6) in addition to the time scale for diffusion. One is the time needed to flush the initial box with one pore volume, t_p, and the other is the characteristic time for reaction, t_k. We have that

$$t_p = \frac{\phi l_0}{u_{D0}} \quad \text{and} \quad t_k = \frac{\phi c_{\rm eq}}{S k_d} \tag{8}$$

so that

$$\mathrm{Pe} = \frac{t_0}{t_p} \quad \text{and} \quad \mathrm{Da} = \frac{t_0}{t_k} \tag{9}$$

The Pe- and Da-numbers, the two parameters in the mathematical model, may be interpreted in terms of the time scales involved. The Pe-number is the characteristic time of the diffusion process relative to the characteristic time of the flow process, and the Da-number is the characteristic time of the diffusion process relative to the characteristic time of the reaction process. The basic behaviour of the model in terms of the Damköhler-number and the Péclet-number is demonstrated in Appendix B.

4. Permeability and specific reactive surface

Both the absolute permeability and the specific reactive surface area are in general functions of the porosity. The permeability will increase with increasing porosity and we assume that log of the permeability is linear in the porosity in the numerical model

$$\log_{10} k(\phi) = a\phi + b. \tag{10}$$

This function has been suggested for shales by Neuzil [12], but it has also been used for wide range of rocks [6]. It has the advantage that it can be used to interpolate between two pairs of porosity-permeability measurements, since it has two parameters a and b. The two pairs can be the porosity-permeability of the initial state and the final state, respectively. Other common choices are the Kozeny-Carman function [19], which suits well sorted clean sandstones, like the Fountainbleau sandstone [2]. Similar to the Kozeny-Carman function is the generalized power-function, where the permeability is proportional to the porosity to the power of a free parameter [7].

The specific reactive surface area is another rock property that depends on the porosity. Ortoleva et al. [14] suggested a function of the form

$$S(\phi) = S_0 \frac{(\phi_f - \phi)^{2/3}}{(\phi_f - \phi_0)^{2/3}} \tag{11}$$

where S_0 is the specific reactive surface at the initial porosity ϕ_0. The final porosity is ϕ_f, and it is attained when all the reactive material is dissolved. The specific reactive surface function (11) was derived for grains of reactive material, where most of the grain surface is in touch with the fluid. We notice that function (11) gives that $S \to 0$ for $\phi \to \phi_f$ as reactive grains go into solution. It is possible to consider the inverse porous media, where the reactive part of the solid and the void are interchanged, $\phi_f - \phi$ becomes ϕ. The inverse porous medium gives a better description of a well cemented pore space, where the pores are "holes" in a solid matrix. The specific reactive surface area function is then

$$S(\phi) = S_0 \cdot \left(\frac{\phi}{\phi_0}\right)^{2/3} \tag{12}$$

and we see that the specific reactive surface area increases as a function of the porosity. The exponent can be introduced as a parameter n

$$S(\phi) = S_0 \cdot \left(\frac{\phi}{\phi_0}\right)^{n} \tag{13}$$

which gives more freedom when calibrating the specific surface area to a particular rock. Colon et al. [5] observed increasing specific surface area with increasing porosity by dissolution of cores of Fontainebleau sandstone. The increase could have been fitted with a linear function $S(\phi) = A\,(\phi - \phi_0) + S_0$. A simple choice for the parameter A, when little is known about the core, is to let $A = S_0/\phi_0$, which then gives (13) for $n = 1$. In the following we assume the specific reactive surface function (13) with the exponent $n = 1$. It should be mentioned that there are large uncertainties associated

with surface-area relationships for real rocks, as for instance observed by Noiriel et al. [13].

A specific choice of a function $S(\phi)$ is not so important as long as it leads to a small change to the rate of change of porosity. The function S increases by a factor in the range from 1 to 3.3 when the porosity increases from 0.15 to 0.5. A notable difference between the specific surface functions (11) and (13) is that the first decreases towards zero when ϕ approaches the final porosity, while the second increases towards a maximum value. It is reasonable that the specific reactive surface is increasing when the pores (the "holes") are increasing, as long as the pore surface is made of reactive material. But at some point, when the specific reactive surface is approaching the final porosity, and nearly all the reactive material is dissolved, the specific surface must approach zero. This is simply achieved in the numerical model by setting the specific reactive surface to zero when the final porosity is reached, and the dissolution process is then stopped.

5. Stability of reaction fronts

It is convenient with respect to the analytical treatment to approximate the zone of reaction as a sharp front in concentration and porosity. The front then divides the pore space into an unreacted part ahead of the front and a reacted part behind the front, see figure 1. All the reactive material has gone into solution behind the front, but no reactive material is dissolved ahead of the front. The reactive transport equation becomes replaced by a step-function in the concentration. The transport is then by Darcy flow and not by diffusion, because the concentration gradient is everywhere zero except at the front.

A simple mass-balance consideration gives that the front then moves with the velocity

$$u_f = N_f\, u_D, \quad N_f = \frac{M_f}{1+\phi_0 M_f} \quad \text{and} \quad M_f = \frac{N_p}{\phi_f - \phi_0} \tag{14}$$

where u_D is the Darcy velocity normal to the front, and where ϕ_0 and ϕ_f are the porosities ahead of and behind the front, respectively. The parameter N_f is a dimensionless coefficient. The derivation of the front velocity (14) is given in Appendix A. Zhao et al. [23] derive the same front velocity by integrating the pressure equation and the concentration equation, after they have been mapped to a coordinate system that follows the front. We notice that the reaction kinetics do not appear in the front velocity. That is because the reaction is assumed to take place so fast that the rate limiting step is Darcy flow. Actually, a sharp front (with zero lateral extent) assumes that the reaction is infinitely fast.

The stability criterion is obtained in a similar manner as for viscous fingering in a Hele-Shaw cell [16, 15, 11]. The derivation uses the same approach as Marle [11], as shown in next section. The unreacted and reacted subdomains are denoted by the indices $i = 1$ and 2, respectively. The equations for each subdomain are

$$\phi = \phi_i, \qquad \nabla \cdot \mathbf{w}_i = 0, \qquad \mathbf{w}_i = -\frac{k_i}{\mu}\nabla p_i, \quad \text{for} \quad i = 1, 2 \tag{15}$$

where $\mathbf{w} = (u_i, v_i)$ is the Darcy flux. The assumption of a sharp reaction front that separates two homogeneous pore spaces leads to constant porosities ϕ_0 and ϕ_f at the opposite sides of the front. Constant porosities give constant permeabilities $k_1 = k(\phi_0)$ and $k_2 = k(\phi_f)$ from the permeability function. A constant porosity and permeability in each subdomain is also assumed in the stability criterion obtained by Chadam et al. [3, 4], Ortoleva et al. [14], Xin et al. [20]. Furthermore, a constant porosity in each subdomain also implies that the concentration is constant in the subdomains as well.

The concentration has the trivial solution $c = 0$ in the reacted part and $c = c_{\mathrm{eq}}$ in the unreacted part.

A similar step function in concentration could have been made that represents precipitation. The argument that leads to the stability criterion applies equally well for precipitation processes as for dissolution processes.

We also need equations at the interface in addition to the equations for each subdomain. At the front we have that

$$p_1 = p_2, \qquad \mathbf{w}_1 \cdot \mathbf{n} = \mathbf{w}_2 \cdot \mathbf{n}, \quad \text{and} \quad u_f = N_f \, u_D \tag{16}$$

where $\mathbf{n}$ is a unit normal vector to the front. The fluid pressure at the front is continuous ($p_1 = p_2$) and the flow of fluid through the front conserves mass ($\mathbf{w}_1 \cdot \mathbf{n} = \mathbf{w}_2 \cdot \mathbf{n}$). Notice that we have Darcy flow through the front, which is a difference compared to the front between two immiscible fluids. The front velocity is u_f and the Darcy flux u_D is in the direction normal to the front. We therefore have $u_D = \mathbf{w}_1 \cdot \mathbf{n} = \mathbf{w}_2 \cdot \mathbf{n}$ at the front.

A linear stability analysis then gives that a small perturbation of the sharp front with wave length λ evolves proportional to the factor $\exp(\theta \, t)$, where

$$\theta = \frac{(k_2 - k_1)}{(k_2 + k_1)} \frac{2\pi}{\lambda} N_f \, u_D. \tag{17}$$

The derivation of factor $\exp(\theta \, t)$ is given in the next section. The sign of the factor θ controls the front stability, since the perturbation grows exponentially when $\theta > 0$. The sign of θ is given by the permeabilities of the subdomains and we have that

$$\begin{aligned} &k_2 > k_1 \quad \text{unstable front: perturbations grow} \\ &k_2 = k_1 \quad \text{labile front: perturbations are preserved} \\ &k_2 < k_1 \quad \text{stable front: perturbations decrease} \end{aligned} \tag{18}$$

The parameter θ is also inversely proportional to the wave-length. This implies that perturbations with short wave-lengths grow faster than perturbations with long wave-lengths, in case of an unstable sharp front. Similarly, short wave-lengths die out faster than long wave-lengths in the stable regime. Another property of θ is that

$$\theta \approx \frac{2\pi}{\lambda} N_f \, u_D \qquad \text{when} \qquad k_2 \gg k_1. \tag{19}$$

The growth of the instability is only weakly dependent on the permeabilities when the reacted area behind the front gets a much higher permeability than the unreacted domain ahead of the front.

The stability criterion is simpler than the one obtained by Chadam et al. [3], Ortoleva et al. [14], Xin et al. [20], Zhao et al. [23]. It is based on a sharp front assumption for porosity, permeability and concentration, while Chadam et al. [3], Ortoleva et al. [14], Xin et al. [20], Zhao et al. [23] assume a sharp front in porosity and permeability, but not in concentration. A sharp front assumption in ϕ (and thereby k) imply an infinite reaction rate at the front, which is also consistent with a sharp front in C. The assumption of a step functions in ϕ, k and C is a consistent set, which is a trivial solution of the reaction-transport model in the limit of an infinite reaction rate.

The growth rate of the instability, θ, can be compared with the results of Sherwood [17] for instability in a model where the reaction rate is finite and where the front has finite width. The model of Sherwood [17] has constant porosity, it ignores diffusion and has a permeability that is inversely proportional to the amount of dissolvable matter. Therefore, the permeability goes towards infinity as the dissolvable matter approaches zero. Sherwood [17] found that $\theta = (u_f/x_0)\log(1 + 2\pi x_0/\lambda)$, which gives that $\theta \approx (2\pi/\lambda)u_f$, for wave lengths much longer than the characteristic length scale $x_0 = u_D/k_d$. The growth rate in the Sherwood [17] model, for the regime $\lambda \gg 2\pi x_0$, is

the same result as the approximation (19).

Hirch and Bhatt [9] have an alternative analysis for a model with finite reaction rate, constant porosity and where they ignore diffusion. They have a reaction term with first order kinetics and they look at stability when the permeability is increasing with the dissolution. They obtained an expression for the growth rate that is equal to equation (17) in the limit of long wave lengths. Wave lengths are long when compared to a characteristic front width similar to x_0. They point out that the condition in the long wave length limit is independent of how the permeability varies with the amount of the dissolvable solid, and that it is only dependent on the upstream and downstream values of the permeability.

The sharp front analysis here does not have a lower limit on the wave length for stability. The models of Sherwood [17] and Hirch and Bhatt [9] also have increasing θ with decreasing wave length, but the behaviour of the models for small wave length differs. The analysis of Sherwood [17] gave that the growth rate of the instability increases as $\approx \log(2\pi x_0/\lambda)$ for small wave lengths, and the growth rate in the model of Hirch and Bhatt [9] approaches a constant value as the wave length goes to zero. The introduction of a dissipation mechanism like diffusion would change that [18]. The review article by Joseph and Saut [10] discuss the problem with short wave length instabilities for a range of processes and regularizing mechanisms. It should also be mentioned that sharp fonts in viscous fingering are stable for wave lengths lower than a critical wave length due to surface tension [11, 24, 25]. Another point is that the sharp front assumption, which assumes infinite fast reaction, is similar to the so-called "mixed-is-burned" analysis for combustion flames, where the reaction is assumed completed at the moment of mixing [18].

6. The derivation of the stability criterion for sharp fronts

The linear stability criterion is studied when a sharp front is assumed. The reaction then goes infinitely fast at the front and the porosity therefore changes as a step-function from its initial value ϕ_0 ahead of the front to its finial value ϕ_f behind the front. The concentration, porosity and permeability in the reacted part behind the front and the unreacted part ahead of the front are therefore 0, ϕ_f, k_2 and $c_{\rm eq}$, ϕ_0, k_1, respectively. The assumption of a sharp front replaces the reaction-transport equation (2) with a step-function in the concentration. The transport is only by convection since the concentration gradient is everywhere zero (except at the front).

The linear stability analysis looks at how a small perturbation of a flat front develops. We let a flat front move with the velocity u_{f0} along the x-axis – the normal vector to the front is parallel to the x-axis. The initial front velocity is related to the initial Darcy flux as $u_{f0} = N_f\, u_{D0}$. The fluid pressure is initially $p_{10}(x)$ and $p_{20}(x)$ before the front is perturbed. The initial Darcy flux in the x-direction gives that the initial fluid pressure gradient is

$$\frac{dp_{i0}}{dx} = -\frac{\mu\, u_{D0}}{k_i} \tag{20}$$

and the initial fluid pressure becomes

$$p_{i0} = -\frac{\mu\, u_{D0}}{k_i}\Big(x - u_{f0}t\Big) \tag{21}$$

for $i = 1, 2$, which has $p_{i0} = 0$ at $x = 0$ at $t = 0$. A reference value for the fluid pressure is arbitrary, and it is conveniently set to zero at the front at time $t = 0$. We will seek a solution for the deviation from the initial state when the linear front is subjected to a small perturbation $h(y, t)$. The fluid pressure and the Darcy flux can then be written as

$$p_i = p_{i0} + p_i' \qquad \text{and} \qquad \mathbf{w}_i = (u_{D0}, 0) + \mathbf{w}_i' \qquad i = 1, 2 \tag{22}$$

where the initial Darcy velocity is

$$(u_{D0}, 0) = \mathbf{w}_0 = -\frac{k_i}{\mu}\nabla p_{i0} \tag{23}$$

and where the primed quantities p_i' and $\mathbf{w}_i'$ are the deviations caused by the perturbation of the front. The equation for the deviation in Darcy flux becomes

$$\mathbf{w}_i' = \mathbf{w}_i - \mathbf{w}_0 = -\frac{k_i}{\mu}\nabla p_i' \quad \text{for} \quad i = 1, 2 \tag{24}$$

and from fluid conservation we get the continuity equation for the deviations in the fluid velocity

$$\nabla \cdot \mathbf{w}_i' = \nabla \cdot (\mathbf{w}_i - \mathbf{w}_0) = 0 \quad \text{for} \quad i = 1, 2. \tag{25}$$

Conservation of fluid through the front, $\mathbf{w}_1 \cdot \mathbf{n} = \mathbf{w}_2 \cdot \mathbf{n}$, gives that

$$\mathbf{w}_1' \cdot \mathbf{n} = \mathbf{w}_2' \cdot \mathbf{n} \tag{26}$$

and continuity of the pressure at the front, $p_1 = p_2$, gives that

$$p_2' - p_1' = -(p_{20} - p_{10}) = \left(\frac{1}{k_2} - \frac{1}{k_1}\right) \mu \, u_{D0} \left(x - u_{f0}t\right) \tag{27}$$

The next step is a change of x-coordinate to $x' = x - u_{f0}t$, which is a coordinate system that follows the initially flat front. The position of the perturbed front in the x'-coordinate system is simply $x' = h(y, t)$, and the velocity of the perturbed front in x'-coordinate system is

$$u_f - u_{f0} = \frac{\partial h}{\partial t} \tag{28}$$

The unit normal vector of the front $x' = h(y, t)$ is

$$\mathbf{n} = \frac{(1, -\partial h/\partial y)}{\left(1 + (\partial h/\partial y)^2\right)^{1/2}} \approx (1, -\frac{\partial h}{\partial y}) \tag{29}$$

when it is approximated to first order in $\partial h/\partial y$. The deviations $\mathbf{w}_i' = (u_i', v_i')$, p_i' and h and their derivatives are infinitesimal quantities, and we have to first order in these quantities that

$$\mathbf{w}_i' \cdot \mathbf{n} \approx u_i' - \frac{\partial h}{\partial y} v_i' \approx u_i'. \tag{30}$$

The equation for the front velocity is

$$\frac{\partial h}{\partial t} = u_f - u_{f0} = N_f \left(u_D - u_{D0}\right) = N_f \, u_i' \tag{31}$$

The first order equations for the infinitesimal deviations are summarized as follows

$$u_i' = -\frac{k_i}{\mu} \frac{\partial p_i'}{\partial x'}, \quad v_i' = -\frac{k_i}{\mu} \frac{\partial p_i'}{\partial y}, \quad \text{and} \quad \frac{\partial u_i'}{\partial x} + \frac{\partial v_i'}{\partial y'} = 0 \tag{32}$$

in each subdomain ($i = 1, 2$), and

$$p_2' - p_1' = \left(\frac{1}{k_2} - \frac{1}{k_1}\right) \mu \, u_{D0} \, h \quad \text{and} \quad \frac{\partial h}{\partial t} = N_f \, u_1' = N_f \, u_2' \tag{33}$$

at the front $x' = x - u_{f0} t = h$. The equations (32) and (33) are supplied by the boundary conditions

$$u_1' = v_1' = p_1' = 0 \quad \text{for} \quad x' \to \infty \tag{34}$$

and

$$u_2' = v_2' = p_2' = 0 \quad \text{for} \quad x' \to -\infty \tag{35}$$

which says that the deviations are zero at an infinite distance away from the front. Following Marle [11], the linear equations (32) and (33) with boundary conditions (34) and (35) are solved with expressions of the following form

$$h(y,t) = A \exp\left(\frac{2\pi j y}{\lambda} + \theta t\right) \tag{36}$$

$$u_i'(x', y, t) = B_i \exp\left(\frac{2\pi j y}{\lambda} + \sigma_i x' + \theta t\right) \tag{37}$$

$$v_i'(x', y, t) = C_i \exp\left(\frac{2\pi j y}{\lambda} + \sigma_i x' + \theta t\right) \tag{38}$$

$$p_i'(x', y, t) = D_i \exp\left(\frac{2\pi j y}{\lambda} + \sigma_i x' + \theta t\right) \tag{39}$$

where $i = 1, 2$ and the $j = \sqrt{-1}$. When these expressions are inserted into equations (32) for the subdomains, we get that

$$B_i = -\frac{k_i}{\mu}\sigma_i D_i, \qquad C_i = -\frac{k_i}{\mu}\frac{2\pi j}{\lambda}D_i, \quad \text{and} \quad \sigma_i B_i + \frac{2\pi j}{\lambda}C_i = 0 \tag{40}$$

and when inserted into the conditions (33) at the front, we have that

$$N_f B_1 = N_f B_2 = A\theta, \quad \text{and} \quad D_2 - D_1 = \Big(\frac{1}{k_2} - \frac{1}{k_1}\Big)\,\mu\, u_{D0} A \tag{41}$$

From equations (40) we get that

$$\sigma_i^2 = \Big(\frac{2\pi}{\lambda}\Big)^2 \tag{42}$$

and the boundary conditions (34) and (35) imply that

$$\sigma_1 = -\frac{2\pi}{\lambda} \quad \text{and} \quad \sigma_2 = \frac{2\pi}{\lambda}. \tag{43}$$

Expression (40) now gives that

$$D_i = -\frac{\mu B_i}{k_i \sigma_i} \tag{44}$$

and therefore

$$D_1 = \frac{\mu\theta A\lambda}{k_1 N_f 2\pi} \quad \text{and} \quad D_2 = -\frac{\mu\theta A\lambda}{k_2 N_f 2\pi} \tag{45}$$

When D_1 and D_2 are inserted into the second equality (41) we have finally that

$$-\Big(\frac{1}{k_2} + \frac{1}{k_1}\Big)\frac{\lambda\theta}{2\pi N_f} = \Big(\frac{1}{k_2} - \frac{1}{k_1}\Big)u_{D0} \tag{46}$$

which gives equation (17) for θ when it is tidied up.

7. Numerical examples

The instability condition (18) is based on the idealization of the front as a step-function in concentration and porosity. This section demonstrates that the instability criterion

may be applied to fronts obtained by a numerical solution of the three coupled reactions (1), (2) and (3). The sharp front assumption can be used assuming that convection dominates diffusion ($\mathrm{Pe} \gg 1$) and that the reaction is sufficiently fast. A standard implicit finite difference scheme has been used, where both the convection term and the source term are treated implicitly. Upstream differencing is applied to the convection term. The three equations have been solved sequentially in time, by solving first for pressure, then for concentration and finally for porosity at each time step. Validations of the numerical concentration and porosity solutions are given in appendices B and C, respectively.

All cases have in common an initial porosity $\phi_0 = 0.15$ and a final porosity $\phi_f = 0.5$, and the dimensionless numbers $\mathrm{Pe} = 800$, $\mathrm{Da} = 2.4 \cdot 10^5$ and $N_p = 0.0075$. One set of parameters for the core scale that gives these $\mathrm{Pe}-$ and Da numbers are $l_0 = 6$ cm, $u_{D0} = 2 \cdot 10^{-6}$ ms^{-1}, $K_d = 0.01$ s^{-1} and $D = 1 \cdot 10^{-9}$ m^{2}s^{-1}. A linear specific surface function (13) and the two-parameter permeability function (10) are used in the simulations. The flow rate is the same in the three cases, and the state of the front is inspected at the same three times $t = 0$, $t = 57.3\, t_p$ and $t = 115\, t_p$, measured in pore volumes. The core could have been a calcite cemented sandstone, where the calcite goes into solution an leaves behind a matrix of quartz grains. The values are not calibrated against one particular core and are only meant for use in a numerical example. Figures 2, 3 and 4 show evolution of the porosity in the core.

The stable case shown in figure 2 has a decreasing permeability from $k_1 = 10^{-15}$ m^2 at $\phi_0 = 0.15$ to $k_2 = 10^{-16}$ m^2 at $\phi_f = 0.5$. We let the permeability decrease, although the porosity increases, in order to give an example of a stable case. Figure 2a shows the initial state of the porosity, before timestepping starts, where the initial front has a

$\sin$-shape. The amplitude is 0.033 and there are 5 wave-lengths in the front. The front is stable in this case, because the permeability is lower behind the front than ahead of the front. Figure 2b shows the expected behaviour where the initial $\sin$-shaped perturbation has died out after a time $57.3\,t_p$. The front then stays flat at later times as seen from figure 2c, which shows the front at time $115\,t_p$.

Figure 3 shows the same case when the permeability is the same at both sides of the front. This is the labile case, and we notice that the front has the same shape as it moves forward.

The last case has the initial permeability increased from $k_1 = 10^{-15}$ m^2 at $\phi_0 = 0.15$ ahead of the front to $k_2 = 10^{-14}$ m^2 at $\phi_f = 0.5$ behind the front. This is the unstable case as seen from figure 4, where the initial $\sin$-shaped perturbation of the porosity grows larger with time.

Figures 2 and 3 allow for a check of the front velocity. (The contour $C = -1/2$ defines the front.) It is then convenient to scale the front velocity (14) by l_0/t_p, which gives the front velocity as $d\hat{x}/d\tau = \phi_0 N_f$, where τ is the dimensionless time t/t_p. We see that the front moves a distance $d\hat{x} \approx 0.18$ during a time interval $d\tau = 57.3$, which gives $d\hat{x}/d\tau \approx 3.1 \cdot 10^{-3}$. The numbers for N_p, ϕ_0 and ϕ_f give that the analytical front velocity is $\phi_0 N_f = 3.2 \cdot 10^{-3}$. The match against the front velocity is good. The limits of the applicability of the stability criterion (18) with respect to large front widths is not covered by the current study.

8. Conclusion

A stability criterion has been derived for reaction fronts driven by Darcy flow, when a sharp front is assumed between the unreacted pore space ahead of the front and the fully reacted pore space behind the front. The stability analysis is considerably simpler than earlier linear stability analyzes, since the only place where reaction takes place is at the front. The stability criterion tells when a perturbation of a sharp front will grow, stay unchanged or decay. The condition is given in terms of the ratio of the permeabilities at the two sides of the front. Perturbations of the sharp front will decay and the front will be stable when the permeability decreases behind the front. The perturbations of the sharp front move unchanged with the front, when the permeabilities are the same at the two sides of the front. Perturbations of the sharp front become unstable for all wave-lengths when the permeability increases behind the front. Short wave-length perturbations grow faster than long wave-length perturbations. The stability of non-sharp fronts are studied numerically. The numerical examples consider dissolution, but other reactions could have been considered, like for instance replacement reactions that change the permeability. These numerical tests are in accordance with the stability criterion based on sharp fronts, and they suggest that the stability criterion may serve as a useful tool in the interpretation of reaction fronts both in the laboratory and in the outcrop.

9. Acknowledgement

This work has been partly funded by the SIS-project at Institute of Energy Technology. The author is grateful to Nina Simon and two anonymous referees for suggestions that improved the manuscript.

Appendix A. The front velocity and the Darcy flux

Figure 5 shows a sharp front that moves a distance dx along the x-axis during a time interval dt. To derive the velocity of a sharp front we will use an observer that travels with the front and sees the porous media pass by. During a time step dt we will see that a volume $dV_r = (\phi_f - \phi_0)\, A\, dx$ goes into solution behind the front, where the area of the front is A. This volume gives the number $dV_r/\mathcal{V}_s$ of moles that goes into solution, where $1/\mathcal{V}_s$ is the molar density. The same number of moles is transported away ahead of the front. The Darcy flux relative to the front is $u_D - \phi_0 u_f$ where $\phi_0 u_f$ is the fluid flux from the front moving with velocity u_f to the right where the porosity is ϕ_0. The fluid volume that leaves the front during the time interval dt is $(u_D - \phi_0 u_f)\, dt\, A$, and the mass balance at the front is therefore

$$(\phi_f - \phi_0)\, A\, dx\, \frac{1}{\mathcal{V}_s} = (u_D - \phi_0 u_f)\, dt\, A\, c_{\text{eq}} \tag{A.1}$$

and by solving for $u_f = dx/dt$ gives the front velocity (14).

There may be a (slightly) larger Darcy flux ahead of the front than behind it due to changing porosity and fluid density by the dissolution process. A similar set-up as above, but with a box fixed with respect to the porous matrix, is used to derive a condition for when this increase is negligible. We consider a box with volume $dV = A\, dx$, during the time interval dt a sharp front needs to pass by, $dx = u_f\, dt$. The total masses inside the volume at the beginning and the end of the time step are

$$M_1 = (1 - \phi_0)\varrho_s\, \Delta V + \phi_0 \varrho_{f,1}\, \Delta V \tag{A.2}$$

$$M_2 = (1 - \phi_f)\varrho_s\, \Delta V + \phi_f \varrho_{f,2}\, \Delta V \tag{A.3}$$

respectively. The fluid density is $\varrho_{f,1}$ ahead of the front, where the fluid has the equilibrium concentration, and it is $\varrho_{f,2}$ behind the front, where the fluid has zero concentration.

The mass difference in the box lead to an increase in the Darcy flux out of the box. The mass increase in the box is equal the net mass inflow, which is

$$M_2 - M_1 = \varrho_{f,2} u_D A\,\Delta t - \varrho_{f,1}(u_D + \Delta u_D) A\,\Delta t \tag{A.4}$$

where the flow out of the box is Δu_D larger than the flow in. Inserting the expressions for M_1 and M_2 into the mass balance at the front (A.4), using that $u_f = dx/dt$, leads to

$$\varrho_{f,1}\Delta u_D = (\varrho_{f,2} - \varrho_{f,1})u_D - (\varrho_{f,2} - \varrho_{f,1})\phi_f u_f + (\phi_f - \phi_0)(\varrho_s - \varrho_{f,1})u_f \tag{A.5}$$

The relative increase in the Darcy flux can be written

$$\frac{\Delta u_D}{u_D} = \frac{\varrho_{f,2} - \varrho_{f,1}}{\varrho_{f,1}}\Big(1 - \phi_f N_f\Big) + \frac{\varrho_s - \varrho_{f,1}}{\varrho_{f,1}}(\phi_f - \phi_0)\, N_f \tag{A.6}$$

where we have used that the front velocity is $u_f = N_f u_D$. The first term in (A.6) represents the change in the flux from a change in the fluid density and second term gives the change in the flux by an increase in the porosity. Assuming that the change in the fluid density is small, $|\varrho_{f,2} - \varrho_{f,1}|/\varrho_{f,1} \ll 1$ and that the front velocity is small compared to the Darcy flux, $N_f \ll 1$, gives that the relative change in the Darcy flux is also small, $\Delta u_D/u_D \ll 1$. For example dissolution of calcite in acid, with the solubility 20 g liter^{-1}, gives that $|\varrho_{f,2} - \varrho_{f,1}|/\varrho_{f,1} < 0.02$. The numerical examples presented in the text has $N_f = 0.021$.

The same reasoning as for Δu_D gives the following expression for conservation of fluid mass

$$\nabla \cdot (\varrho_f \mathbf{u}_D) = -\frac{\partial}{\partial t}\Big((1-\phi)\varrho_s + \phi\varrho_f\Big) \tag{A.7}$$

which also imply that the contribution to the fluid flow from the right-hand-side (the source term) in equation (A.7) is negligible under the conditions above. The source term can be approximated by zero under these conditions.

Appendix B. Verification of the numerical concentration solution

It does not appear to be any non-trivial solution of the coupled system of equations (1), (2) and (3) for the pressure, concentration and porosity. The validation of the numerical solutions for concentration and porosity are therefore done separately. The numerical solution for concentration is tested when the porosity does not change ($\hat{\phi} = 1$), and the numerical porosity solution is tested when the concentration does not change through time.

The numerically computed concentration can be compared with a 1D solution of the stationary reaction-transport equation when the porosity is constant. This is of course not a test of the full solution of the system, but it is nevertheless a useful test of the computation of the concentration. It is a simple stand-alone test of the numerical computation of concentration, especially when it is not a sharp front. Furthermore, such a stationary solution demonstrates the interpretations of the solution in terms of the Damköhler-number and the Péclet-number.

It is straightforward to solve the 1D stationary (time-independent) version of the dimensionless concentration equation (6). The solution is

$$C(\hat{x}) = C_{\text{in}} \frac{\exp(A_2 + A_1\hat{x}) - \exp(A_1 + A_2\hat{x})}{\exp(A_2) - \exp(A_1)} \tag{B.1}$$

where

$$A_{1,2} = \frac{1}{2}\Big(\text{Pe} \pm \sqrt{\text{Pe}^2 + 4\text{Da}}\Big) \tag{B.2}$$

when the boundary conditions are $C = C_{\text{in}} = -1$ at $\hat{x} = 0$ and $C = 0$ at $\hat{x} = 1$. There are two interesting end-members of the stationary solution (B.1), one of which is convection dominated ($\text{Pe} \gg 2\sqrt{\text{Da}}$), and the other, which is reaction dominated

($\mathrm{Da} \gg \frac{1}{4}\mathrm{Pe}^2$). The parameters A_1 and A_2 are then

$$A_1 \approx \mathrm{Pe}, \quad A_2 \approx 0 \quad \text{for} \quad \mathrm{Pe} \gg 2\sqrt{\mathrm{Da}} \tag{B.3}$$

and

$$A_1 = \sqrt{\mathrm{Da}}, \quad A_2 = -\sqrt{\mathrm{Da}} \quad \text{for} \quad \mathrm{Da} \gg \frac{1}{4}\mathrm{Pe}^2. \tag{B.4}$$

The convection dominated regime depends almost only on the Pe-number and the reaction dominated regime depends almost only on the Da-number. Figure 6 demonstrates the two regimes. The convection dominated regime, $\mathrm{Pe} \gg \mathrm{Da}$, shows that the fluid flows through the system sufficiently fast to avoid much reaction with the solid. The initial concentration is therefore almost unchanged. In the reaction dominated regime, $\mathrm{Da} \gg \frac{1}{4}\mathrm{Pe}^2$, reaction happens sufficiently fast compared to transport that the fluid reaches equilibrium close to the inlet. Figure 6 also shows the numerical solution for these cases after 5 pore volumes have flushed the system and the numerical solution is in good agreement with the analytically stationary solution (B.1).

The stationary solution is normally attained in much less than one pore volume for the regime $\mathrm{Pe} \gg 2\sqrt{\mathrm{Da}}$. The transient regime at the beginning of flooding is not tested, but this regime is not so important either for experiments that need several or may be a large number of pore volumes to move the front a substantial distance compared to l_0.

Appendix C. Simple verification of the numerical porosity solution

The porosity equation (3) can be made dimensionless using the same scaling as the concentration equation. It is assumed that the specific reactive surface, as a function of porosity, is given by function (13). The time-rate of change of porosity then becomes

$$\frac{\partial \hat{\phi}}{\partial \hat{t}} = -\mathrm{Da}\, N_p\, C(\hat{x}, \hat{t})\, \hat{\phi}^n \tag{C.1}$$

where $\hat{\phi} = \phi/\phi_0$ and $N_p = \mathcal{V}_s c_{\mathrm{eq}}$. The number N_p is the volume of solid dissolved in a unit volume of the reactive fluid. The Da-number (7) is based on the initial porosity ϕ_0.

There are no simple non-trivial solutions of the coupled system of transport, reaction and dissolution. A simple way to check the numerical porosity calculation is to use the stationary solution (B.1) in the rate of change of porosity (C.1). It is then straightforward to integrate (C.1) when the concentration is independent of time, and we have that

$$\hat{\phi}(\hat{x},\hat{t}) = \frac{\phi}{\phi_0} = \begin{cases} \exp\Big(-\mathrm{Da}\, N_p\, C(\hat{x})\,\hat{t}\Big), & n = 1 \\ \Big(1 + (n-1)\,\mathrm{Da}\, N_p\, C(\hat{x})\,\hat{t}\Big)^{1/(n-1)}, & n \neq 1 \end{cases} \tag{C.2}$$

This is just a separate test of the numerical porosity solution and it is not a solution of the full system of equations, because it is based on the stationary solution (B.1). Figure 7 compares the numerical porosity solution, when the porosity in the numerical reaction-transport equation is kept constant, with the porosity solution (C.2). The comparison against the test solution (C.2) is good. The case shown in figure 7 has $\mathrm{Da} = 5 \cdot 10^3$, $\mathrm{Pe} = 10^3$ and $N_p = 1.875 \cdot 10^{-3}$, and the porosity is plotted at (a) $t = 100\,t_p$, (b) $t = 300\,t_p$, (c) $t = 500\,t_p$, (d) $t = 700\,t_p$ and (e) $t = 900\,t_p$ pore volumes.

References

[1] Bear, J., Dynamics of fluids in porous media, American Elsevier, New York (1972)

[2] Bourbie, T., Zinszner, B., Hydraulic and acoustic properties as a function of porosity in Fontainebleau sandstone, Journal of Geophysical Research 90 (1985) 11,524–11,532

[3] Chadam, J., Hoff, D., Merino, E., Ortoleva, P., Sen, A., Reactive infiltration instabilities, IMA Journal of Applied Mathematics 36 (1987) 207–220

[4] Chadam, J., Ortoleva, P., Sen, A., A weakly nonlinear stability analysis of the reactive infiltration interface, SIAM Journal on Applied Mathematics 48 (1988) 1362–1378

[5] Colon, C.F., Oelkers, E.H., Schott, J., Experimental investigation of the effect of dissolution on sandstone permeability, porosity, and reactive surface area, Geochimica et Cosmochimica Acta 68, 4, (2004) 805–817

[6] Corbet, T., Bethke, C., Disequilibrium fluid pressures and groundwater flow in western Canada sedimentary basin, Journal of Geophysical Research 97 (1997) 7203–7217

[7] David, C., Wong, T., Zhang, J., Laboratory measurement of compaction-induced permeability change in the porous rocks: Implications for the generation and maintenance of pore pressure excess in the crust, Pageoph. 143 1/2/3 (1994) 425–456

[8] Golfier, F., Zarcone, C., Bazin, B., Lenormand, R., Lasseux, D., Quintard, M., On the ability of a darcy-scale model to capture wormhole formation during the dissolution of a porous medium, Journal of Fluid Mechanics 457 (2002) 213–254.

[9] Hirch, E.J., Bhatt, B.S., Stability of an acid front moving through porous rock, Journal of Fluid Mechanics 212 (1990) 279-288

[10] Joseph, D.D., Saut, J.C., Short-wave instabilities and ill-posed initial value problems, Theoretical and Computational Fluid Dynamics 1 (1990) 191–227

[11] Marle, C., Multiphase flow in porous media, Editions Technip (Paris) (1981)

[12] Neuzil, C., How permeable are clays and shales? Water Resources Research 30 (1994) 145–150

[13] Noiriel, C., Luquot, L., Made, B., Raimbault, L., Gouze, P., van der Lee, J., Changes in reactive surface area during limestone dissolution: An experimental and modelling study, Chemical Geology 265 (2009) 160–170

[14] Ortoleva, P., Chadam, J., Merino, E., Sen, A., Geochemical self-organization II; the reactive-infiltration instability, American Journal of Science 287 (1987) 1008–1040

[15] Saffman, P., Exact solutions for the growth of fingers from a flat interface between two fluids in a porous medium or Hele-Shaw cell, Quarterly Journal of Mechanics and Applied Mathematics 12 (1959) 146–150

[16] Saffman, P., Taylor, G., The penetration of a fluid into a medium of Hele-Shaw cell containing a more viscous liquid, The Proceedings of the Royal Society of London, A 58 (1958) 245–312

[17] Sherwood, J.D., Stability of a plane reaction front in a porous medium, Chemical Engineering Science 42 (1987) 1823-1829

[18] Sivashinsky, G.I., Instabilities, pattern, and turbulence in flames, Annual Review of Fluid Mechanics 15 (1983) 179-227

[19] Wangen, M., Physical principles of sedimentary basin analysis, Cambridge University Press (2010)

[20] Xin, J., Peirce, A., Chadam, J., Ortoleva, P., Reactive flows in layered porous-media II. The shape stability of the reaction interface, SIAM Journal on Applied Mathematics 53 (1993) 319–339

[21] Xu, T., Apps, J., Pruess, K., Reactive geochemical transport simulation to study mineral trapping for CO2 disposal in deep arenaceous formations, Journal of Geophysical Research 108 (2003) 2071

[22] Xu, T., Apps, J., Pruess, K., Mineral sequestration of carbon dioxide in a sandstone-shale system, Chemical Geology 205 (2005) 295–318

[23] Zhao, C., Hobbs, B., Hornby, P., Ord, A., Peng, S., Liu, L., Theoretical and numerical analyses of chemical-dissolution front instability in fluid-saturated porous rocks, International Journal for Numerical and Analytical Methods in Geomechanics 32 (2008) 1107–1130

[24] Zimmerman, W.C., Homsy, G.M., Nonlinear viscous fingering in miscible displacement with anisotropic dispersion. Physics of Fluids A 3(8) (1991) 1859–1872

[25] Zimmerman, W.C., Homsy, G.M., Three-dimensional viscous fingering: A numerical study, Physics of Fluids A 4(9) (1992) 1901–1914

Captions

Figure 1. A sketch of the reaction front. Fluid flow is towards the right. The area i=1 is the unreacted part ahead of the front and i=2 is the reacted part behind the front.

Figure 2. (a) The initial $\sin$-shaped perturbation in the porosity. (b) The initial perturbation has died out at $t = 57.3\, t_p$. (c) The front remains flat at later time $t = 115\, t_p$.

Figure 3. (a) The initial $\sin$-shaped perturbation in the porosity. (b) and (c) The initial perturbation is preserved at later times $t = 57.3\, t_p$ and $t = 115\, t_p$.

Figure 4. (a) The initial $\sin$-shaped perturbation in the porosity. (b) The initial perturbation has grown considerably at time $t = 57.3\, t_p$; (c) and it has grown even more at later time $t = 115\, t_p$.

Figure 5. The front moves a distance dx during the time interval dt. The porosity ahead of the front is ϕ_0 and it is ϕ_f behind the front. The Darcy flux is u_D on both sides of the front.

Figure 6. The numerical solution of concentration is compared with the stationary solution, when there is no feedback on the porosity.

Figure 7. The simple test of the numerical porosity computation.

Figures

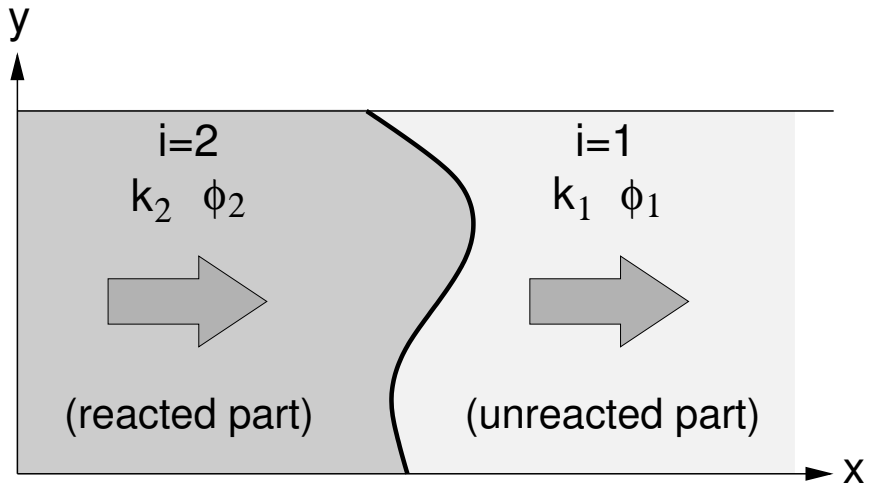

Figure: 1 (file: fig1.eps)

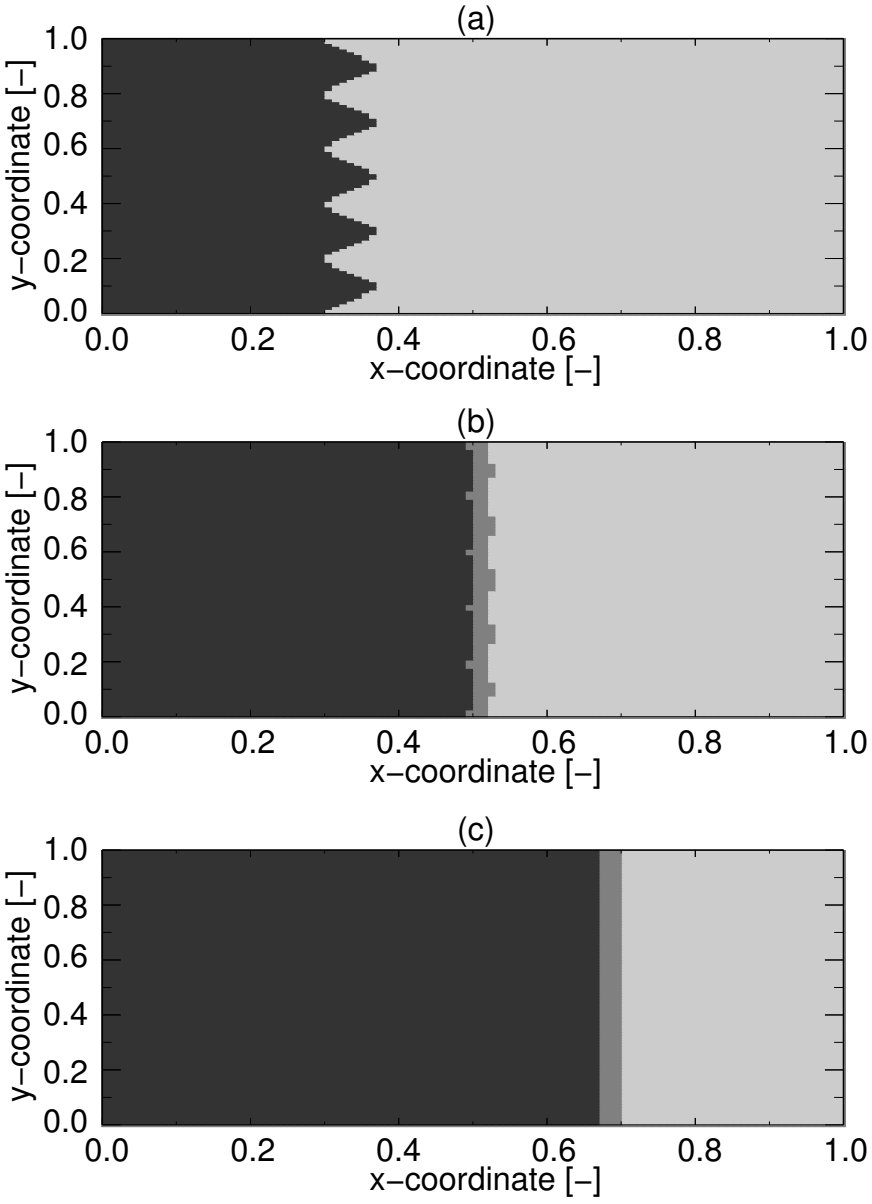

Figure: 2 (file: fig2.eps)

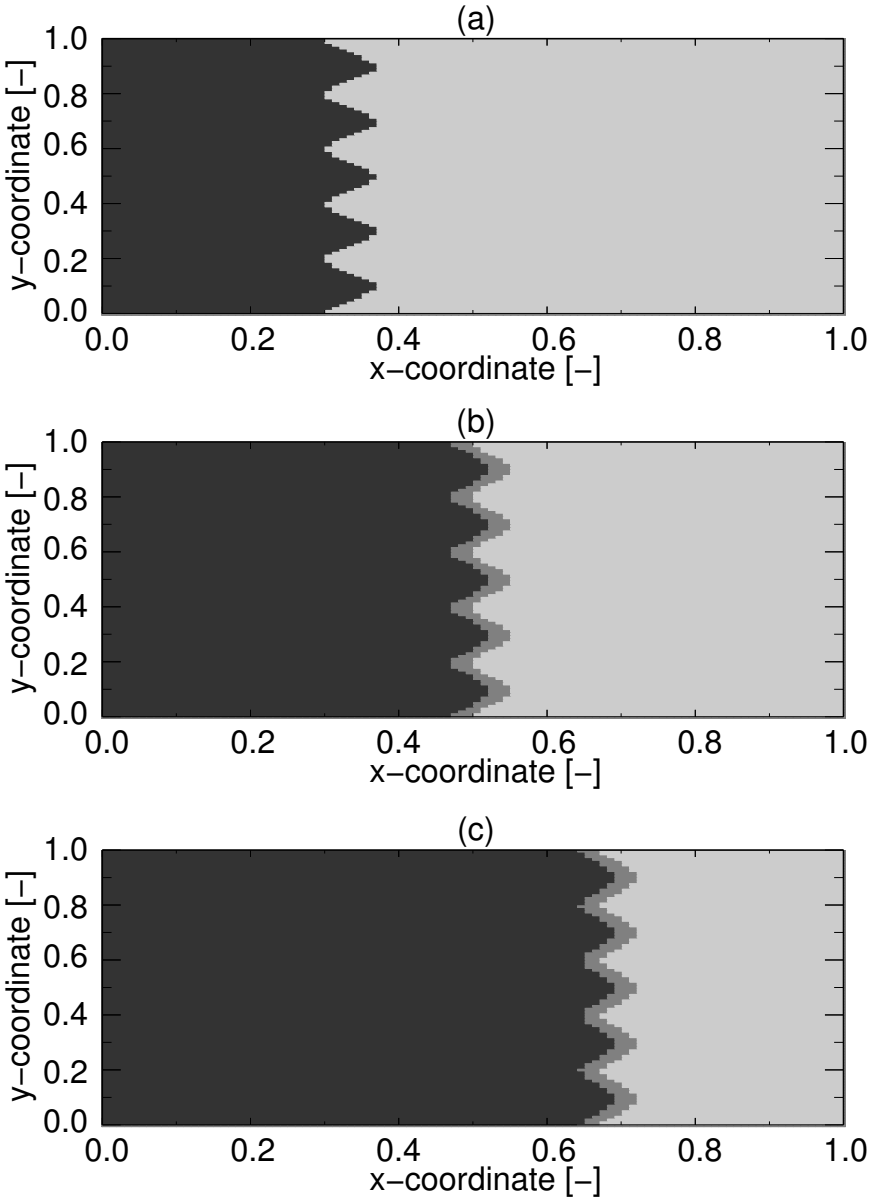

Figure: 3 (file: fig3.eps)

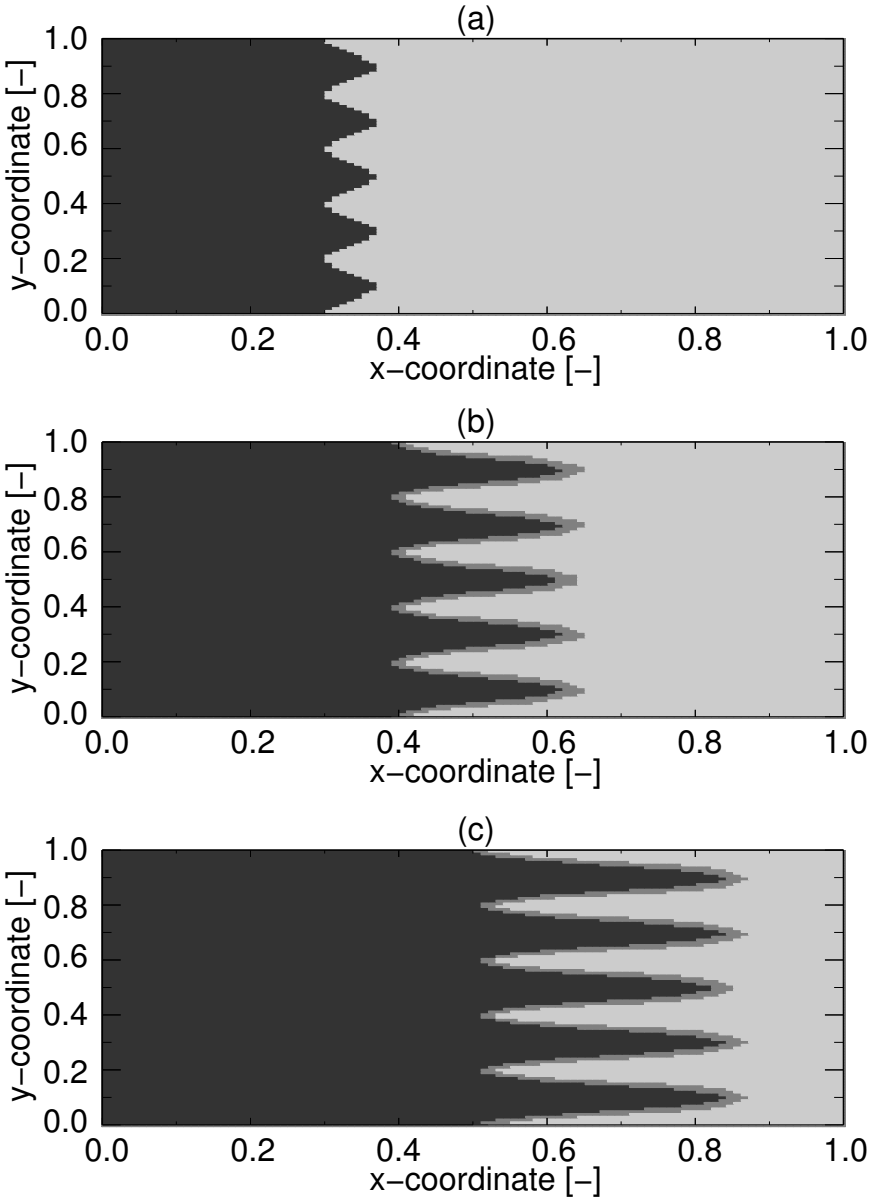

Figure: 4 (file: fig4.eps)

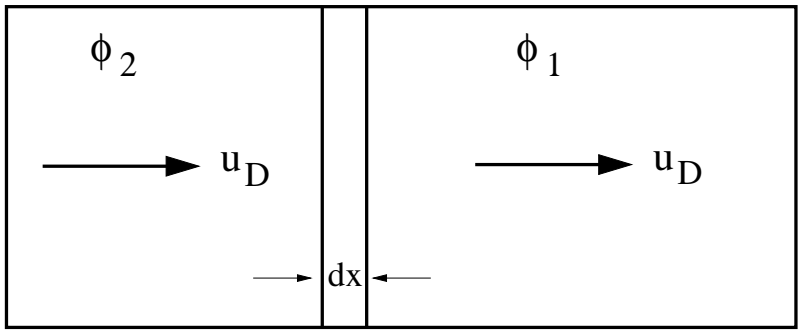

Figure: 5 (file: fig5.eps)

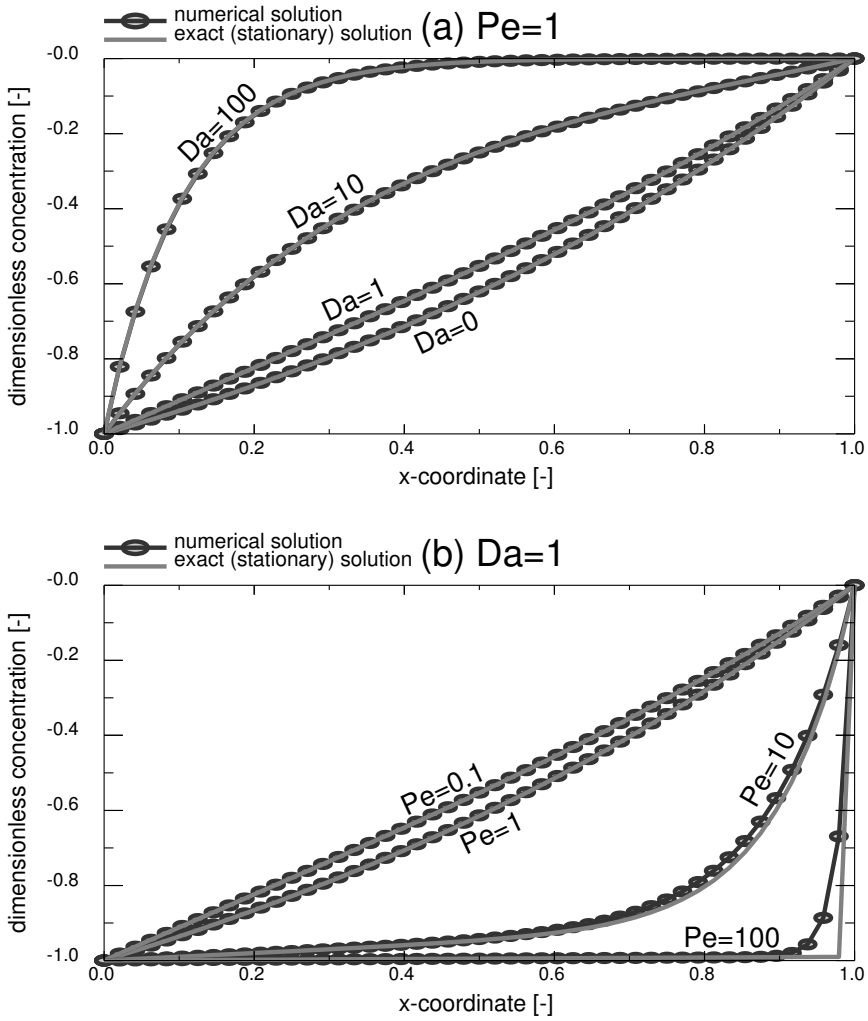

Figure: 6 (file: fig6.eps)

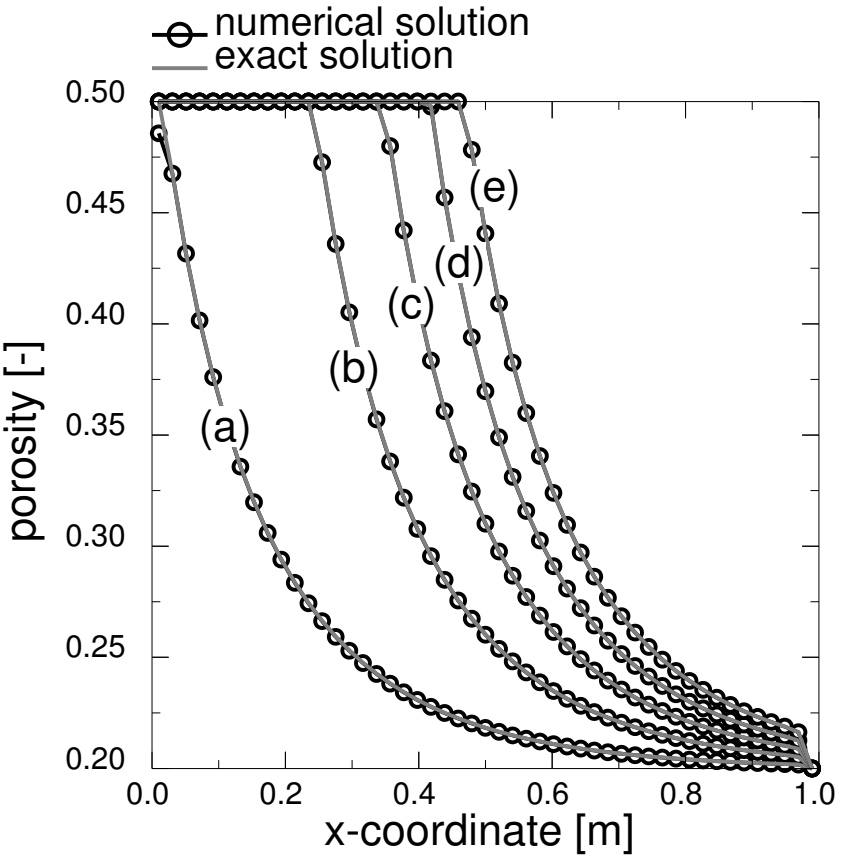

Figure: 7 (file: fig7.eps)